View metadata, citation and similar papers at core.ac.uk

brought to you by CORE

provided by Elsevier - Publisher Connector

Alexandria Engineering Journal (2015) 54, 155–162

HOSTED BY

ELSEVIER

Alexandria University

Alexandria Engineering Journal

www.elsevier.com/locate/aej
www.sciencedirect.com

ORIGINAL ARTICLE

Performance analysis of octal rings as mechanical force transducers

Essam Soliman [1]

Department of Mechanical Engineering, Salman AbdulAziz University, Saudi Arabia

Received 23 August 2014; revised 15 January 2015; accepted 18 January 2015
Available online 12 February 2015

KEYWORDS

Octal rings;
Strain gauge;
Average strain;
Sensitivity;
Stiffness;
Force transducer

Abstract The present work analyzes the characteristics of octal rings as mechanical force transducers. It uses a finite element model of the ring to determine its state of strain upon the application of load. It also correlates ring design parameters and performance measures, using an L_9 orthogonal array of finite element simulations. Design parameters include height, thickness, width, and edge curvature. Performance measures include sensitivity and stiffness. Model simulation results showed a considerable variation in strain along ring face with a considerable difference in the maximum values of the tensile and compressive strains. They, also, revealed a region of a large tensile strain within the ring not addressed in the literature. Moreover, simulation results showed that increasing ring height and decreasing its thickness increases its sensitivity and decreases its stiffness. The width of the ring does not have clear effect of stiffness. However, increasing width decreases sensitivity. Ring edge radius has no significant effect on sensitivity while increasing the edge radius decreases stiffness. A developed relation between strain gauge length and average strain revealed an optimal gauge length that improves ring performance.
© 2015 Faculty of Engineering, Alexandria University. Production and hosting by Elsevier B.V. This is an open access article under the CC BY-NC-ND license (http://creativecommons.org/licenses/by-nc-nd/4.0/).

1. Introduction

Mechanical force measurement has a wide range of applications. They include weighing systems, material testing, and performance evaluation of equipment. In addition, mechanical force measurement is essential for performance improvement and optimization of machining processes, tool breakage detection and chatter control. Moreover, prediction of chip loading and accuracy of machined surface rely on mechanical force measurement.

Mechanical forces are measured indirectly using two main techniques; in the first one, the force acts on a piezoelectric crystal that accumulates charge proportional to the magnitude of the force. A charge amplifier, then, converts charge to volt. In general, piezoelectric sensors are very sensitive to mechanical forces and have wide bandwidth, over 50 kHz. They are available in different configurations and sensitivities. In addition, charge amplifiers are available in wide range of configuration and characteristics. However, they are expensive, delicate and require a considerable attention when used within the harsh machining environment. They are susceptible to

[1] On leave, from Department of Production Engineering, Faculty of Engineering, Alexandria University.

Peer review under responsibility of Faculty of Engineering, Alexandria University.

http://dx.doi.org/10.1016/j.aej.2015.01.004
1110-0168 © 2015 Faculty of Engineering, Alexandria University. Production and hosting by Elsevier B.V.
This is an open access article under the CC BY-NC-ND license (http://creativecommons.org/licenses/by-nc-nd/4.0/).

noise from nearby electrical drives. Therefore, the present work will not consider piezoelectric sensors.

In the second technique, the force acts on an elastic mechanical member. The strain and deflection of the member are proportional to force. A common mechanical member for force measurement is octal ring. A strain gauge converts strain in the strain ring into equivalent volt using a bridge. Octal rings are easy to manufacture to the required size. Strain gauges are relatively inexpensive and are available in a wide range of configurations and characteristics. In addition, bridges, in particular Wheatstone bridge, are easy to operate and maintain. Therefore, octal rings with strain gauges are the candidate for sensing mechanical forces in the present work.

2. Previous research

A considerable amount of research work focused on analyzing performance characteristics of octal rings. The purpose was to use them as force transducers for constructing force dynamometers. Korencke and Hull [1] developed empirical formulae to describe strain, stress and deflection in octal rings. They used ANSYS finite element model and a nonlinear regression model to develop the equations. The developed equations provided close results to experimental data compared to equations available from thin ring theory. However, validity of equations was limited to range of ring thickness and width.

Kim and Kim [2] developed a combined type tool dynamometer for an ultra-precise lathe. They used strain gauges to measure the static force and a piezo-electric film accelerometer to measure the dynamic force. They pointed out that signal conditioning and processing are essential for improving accuracy of force measurement.

Seker et al. [3] used a bending beam type dynamometer to measure machining force for the shaping process. Even though the authors designed the dynamometer, they did not give enough details of its construction. They gave the general characteristics of the load cell used. They focused on the measured force data rather than on the design of the dynamometer. They used cutting force data to correlate cutting parameters, including depth of cut and feedrate, to process performance measures including surface roughness of work part and tool life.

Korkot and Karabay [4,5] used octal strain rings to design milling and drilling dynamometers. They used approximate equations to estimate strain and stiffness in octal rings. They claimed that the dynamometers could measure cutting force with ± 5 N sensitivity and 0.05% or less cross-sensitivity. They presented no information regarding strain gauge type or dimensions. In addition, they did not show clearly the procedure for recording and processing signals from the dynamometers.

Yaldiz and Unsacar [6,7] designed a three-component force dynamometer for the measurement of cutting force in turning. They, also, used octal rings as sensing element and used approximate equations from the thin ring theory to design the rings. The range of the measured force was 3500 N. Sensitivity was ± 5 N and cross-sensitivity was 0.17–0.92%. Length of strain gauge was 6 mm, about 30% of the length of the octal ring face, which was 16.6 mm.

Chen et al. [8] used extended octal rings and strain gauges to design a dynamometer for a tractor drawbar. They used finite element analysis to determine points of maximum strain and fixed strain gauges at these points to get maximum possible sensitively of the dynamometer. However, they did not consider strain distribution around points of maximum strain.

Karabay [9–11] used strain gauges with different forms of octal strain rings to design force dynamometers for the drilling and milling processes. They used equations from the thin ring theory for the design of the rings. No attention was given to strain distribution along the area where strain gauges were fixed. They used calibration to correlate signal from a strain gauge bridge and cutting forces.

Yalidz et al. [12] used octal rings and strain gauges to design a force dynamometer for the milling process. They determined the dynamic characteristics of the dynamometer using the impact test. They showed that the natural frequencies of the dynamometer were low. The only extra feature in their design was using large number of strain gauges to increase dynamometer sensitively.

This work considers octal rings as sensing element for measuring mechanical force. The aim of the work was to investigate strain distribution along the different faces and regions of the ring, with the purpose of deciding on the best area on the ring to adhere strain gauges to end up with maximum possible sensitivity to mechanical force. In addition, this work, considers the correlation between design parameters of the ring and its performance measures.

3. Geometric model

In order to study the state of strain of octal rings, a 3D geometrical model of a ring was constructed using the Solid Edge Software package. Fig. 1 shows the model. The basic design parameters are height, H, width, W, thickness, T, and edge radius R. Other parameters such as face length, L_s and inner hole diameter, D, are derived from the basic design parameters. Then, the finite element method was applied to the model using the same software package. Tetrahedral finite elements were used for the finite element model as shown in Fig. 1. The material of the ring was selected to be Aluminum 1060 with 68.947 GPa modulus of elasticity, 0.33 Poisson ratio, 27.579 MPa yield stress and 68.948 MPa ultimate tensile strength. Fig. 1, also, shows faces and regions of interest where maximum strains or maximum deformations are expected to take place.

A concentrated force, F_z, is applied normal to the face Cu_{out}, in the negative z-direction. The concentrated force represents the worst loading condition of the ring considering deflection and ring stiffness. The magnitude of the force is selected to be $F_z = 100$ N. Such selection ensures no plastic deformation takes place within the ring for the range of design parameters used for the present work and given in the next section. The model considers a ring rigidly fixed at its bottom surface. This simulates a ring welded to its base. The method of fixation of the ring affects mainly state of strain around the fixation region. However, interest is in strains at faces and regions away from ring bottom. In addition, the applied force tends to fix the bottom face of the ring to its base. Therefore, this work does not give the method of fixation a considerable attention.

Upon application of the load and simulating the model, strains of all surface finite elements of the ring were available. Strains at the elements within the aforementioned faces and regions of interest were recorded manually using a strain pick

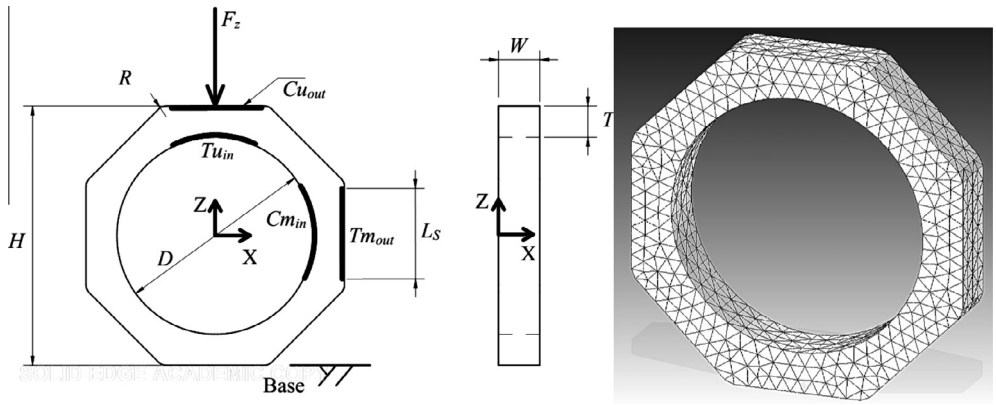

Figure 1 Geometric and finite element models and basic design parameters of the octal ring.

feature of the software. In addition, the positions of the elements, with respect to the *XYZ* coordinate system of Fig. 1, were recorded and stored in data structures within the MATLAB software. All strains, deformations and stresses, were recorded in the *ZX*-plane.

4. Design of simulations

Performance measures of an octal ring are mainly sensitivity and stiffness. Sensitivity, S_z, is defined as:

$$S_z = \frac{\varepsilon^{\max}}{F_z} \tag{1}$$

where F_z is the force acting on the ring and $\varepsilon_{\max}$ is the maximum measurable strain in the ring.

Similarly, stiffness, K_z, of the ring is defined as:

$$K_z = \frac{F_z}{\alpha^{\max}} \tag{2}$$

where $\alpha_{\max}$ is the maximum measurable deflection at the Cu_{out} surface of the ring, basically, at the point of application of the load.

The suffix z in Eqs. (1) and (2) indicates that sensitivity and stiffness are determined in the z-direction. Sensitivity and stiffness of the ring in the x-direction can be dealt with in the same way as in z-direction and, therefore, are not considered in the present work.

Finite element simulations were conducted to correlate the design parameters and the performance measures. Simulation design parameters followed an L_9 orthogonal array. Table 1 shows the levels of design parameters for the simulations. The table also gives the values of the derived parameters.

Because the size of the ring varies from one simulation to another, the number of finite elements, N_f, and number of nodes, N_n, for the finite element model vary as well. Finite element size, E_s, is selected to give reasonably smooth strain distribution. Table 1 gives values of finite element model parameters.

5. Results and discussions

Fig. 2a shows strain distribution along the face Tm_{out} for SIM 2. The dashed line represents the ring profile while the solid line represents the strain distribution. The strain, ε_t, is in tension state and therefore, has positive values in the figure. The figure also shows the z-positions of the element of Tm_{out} at which ε_t is recorded. It can be observed from the figure that the strain varies considerably along the face and the max strain, $\varepsilon_t^{\max} = 67.7$ [μm/m], is almost seven times larger than the minimum strain, 10 [μm/m]. Fig. 2c is an enlarged view of Fig. 2a, around the middle of Tm_{out} where the z-position is zero. It can be observed from the figure that $\varepsilon_t^{\max}$ is shifted from the center of Tm_{out} by 1.14 [mm]. The shift value corresponds to 6% of the length of Tm_{out}, L_s. In the literature [5,6], $\varepsilon_t^{\max}$ is usually considered at the middle of Tm_{out}. Fig. 2b shows strain distribution over the region Cm_{in} for the same simulation, SIM 2. Again, the dashed line represents the ring profile while the solid line represents strain distribution. The strain, ε_c, is in compression state, and is represented by negative values. The figure also gives the z-position of the elements of Cm_{in} at which ε_c is recorded. From figure, it can be observed that $\varepsilon_c^{\max}$ is 100.9 [μm/m] which is 63% larger than $\varepsilon_t^{\max}$. Fig. 2d is also an enlarged view of Fig. 2b around the zero z-position. It shows that $\varepsilon_c^{\max}$ is shifted by 0.77 [mm] from the zero z-position.

The distributions of ε_t and ε_c and the consequent observations are the same for all simulations. Strain ε_c is always larger, in absolute value, than ε_t. Also, both $\varepsilon_t^{\max}$ and $\varepsilon_c^{\max}$ are shifted from the zero z-position by different values. Table 2 summarizes the results of all simulations for $\varepsilon_t^{\max}$ and $\varepsilon_c^{\max}$ values and the corresponding shift values.

The implication of the aforementioned observations is nonlinear relation between the load and output volt of any force sensor that uses octal rings as transducers. It is common to give force sensor maximum nonlinearity as a sensor specification. Understanding the source of such nonlinearity helps in reducing it and thus improving sensor performance.

Fig. 3 shows strain, ε_u, along Tu_{in} and the x-positions of the finite elements on Tu_{in} at which ε_u values are recorded, for SIM 2. The strain, ε_u, is in tensile state. The maximum value of ε_u, $\varepsilon_u^{\max} = 118.8$ [μm/m], is located at the zero x-position. Table 2 lists the values of $\varepsilon_u^{\max}$ for all simulations. The shift values of $\varepsilon_u^{\max}$ are always zero and, therefore, are not listed in the table.

Looking at Table 2, it can be observed that the values of $\varepsilon_u^{\max}$ are considerably larger than those of $\varepsilon_t^{\max}$ and are relatively larger than the values of $\varepsilon_c^{\max}$. As a result, it is better to employ $\varepsilon_u^{\max}$ and $\varepsilon_c^{\max}$ for the arms of any bridge used with the octal ring. This is because their large values, compared to the values of $\varepsilon_t^{\max}$, will result in a higher strain sensitivity

Table 1 Levels of design parameters.

SIM	Design parameters				Derived parameters		Finite element simulation parameters		
	H (mm)	T (mm)	W (mm)	R (mm)	L_s (mm)	D (mm)	N_f	N_n	E_s (mm)
1	50	4	6	0	20.71	42	66,094	100,153	0.37
2	50	6	8	2	19.05	38	29,845	137,987	0.37
3	50	8	10	4	17.40	34	497,094	714,962	0.22
4	40	4	8	4	13.26	32	89,529	133,056	0.33
5	40	6	10	0	16.57	28	169,484	246,681	0.30
6	40	8	6	2	14.91	24	151,830	221,996	0.29
7	30	4	10	2	10.77	22	495,333	708,939	0.16
8	30	6	6	4	9.11	18	153,450	223,804	0.23
9	30	8	8	0	12.43	14	266,732	376,408	0.37

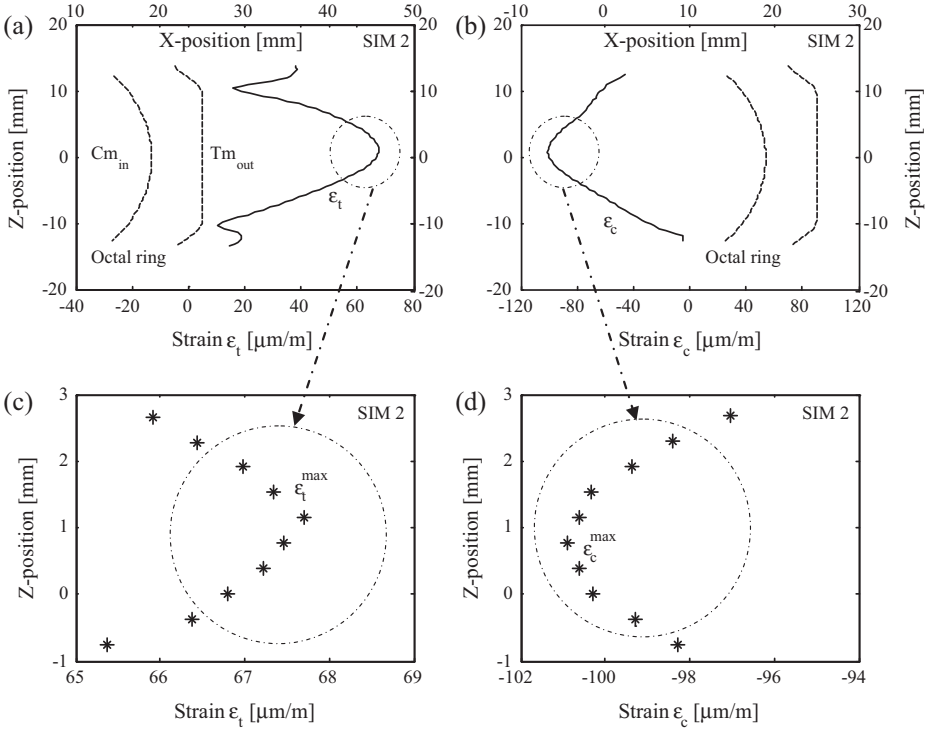

Figure 2 Strain distribution, along Tm_{out} and Cm_{in} for SIM 2.

Table 2 Maximum strain and deflection values and performance measures.

SIM	$\varepsilon_t^{\max}$ (μm/m)	Shift t (mm)	$\varepsilon_c^{\max}$(μm/m)	Shift c (mm)	$\varepsilon_u^{\max}$(μm/m)	$\alpha^{\max}$ (m)	$K_z \times 10^6$ (N/m)	S_z (μm/m/N)
1	218.6	0.74	282.2	1.09	347.7	35.1	2.489	3.48
2	67.7	1.14	100.9	0.77	118.8	8.8	11.363	1.19
3	28.2	1.12	48.9	0.89	55.0	3.3	30.303	0.55
4	134.2	0.66	179.6	0.33	228.5	15.9	6.289	2.29
5	39.3	0.59	65.0	0.30	69.7	3.7	27.027	0.7
6	32.2	0.57	70.1	0.84	71.5	2.9	34.482	0.72
7	73.8	0.63	107.3	0.48	125.7	5.4	18.518	0.13
8	46.1	0.46	95.3	0.67	102.7	3.2	31.25	1.03
9	12.7	0.41	42.3	0.41	35.3	1	100	0.35

to the applied load. However, nonlinearity is unavoidable at this stage.

Fig. 3, also, shows the distribution of the deflections, α, along the face Cu_{out}. The deflection is given for finite elements of Cu_{out} at different x-positions. From the figure, it can be seen that the maximum deflection, $\alpha^{\max}$, is 9 [μm] and is located at the zero x-position. The corresponding stiffness, K_z, is $11.363 * 10^6$ N/m. The distributions of α and ε_u are similar

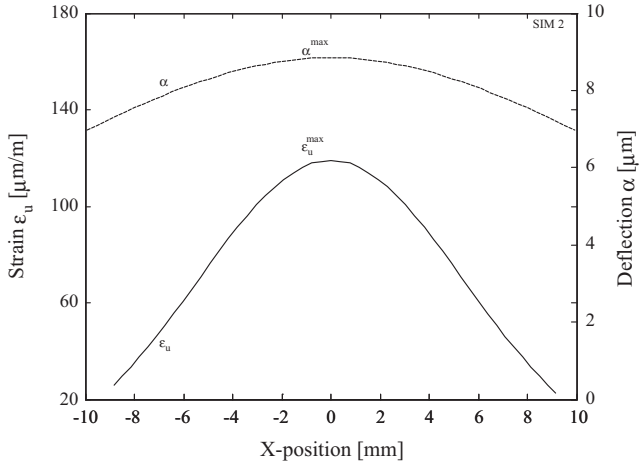

Figure 3 Strain and deflection distributions along Tu_{in} and Cu_{out} respectively.

for all simulation and $\alpha^{\max}$ is always at zero x-position. Table 2 lists all values of $\alpha^{\max}$ for all simulations. It also lists all calculated values of K_z and S_z for all simulations using Eqs. (1) and (2). The S_z values listed in Table 1 are calculated based on $\varepsilon_u^{\max}$ values for $F_z = 100$ N.

To analyze the effect of the different levels of the design parameters on $\varepsilon_{t,c,u}^{\max}$, the variation of means method is employed. The method implies calculating the average values of $\varepsilon_{t,c,u}^{\max}$ for each level of each design parameter. Then, the average values are compared by plotting them as shown in Fig. 4. The figure shows that increasing H increases $\varepsilon_{t,c,u}^{\max}$ values while increasing T and W decreases $\varepsilon_{t,c,u}^{\max}$ values. In addition, the figure shows that R does not have a direct effect on $\varepsilon_{t,c,u}^{\max}$. Moreover, the figure shows that $\varepsilon_c^{\max} and \varepsilon_u^{\max}$ get close to each other as T increases and as H decreases. These results are similar to the theoretical results available in the literature. In fact, the theoretical values of $\varepsilon_t^{\max}$ and $\varepsilon_c^{\max}$ were calculated for all simulation using Eqs. (3) and (4) [6,7]. Eq. (3) is for circular rings, and strain is designated by the superscript "c" while Eq. (4) is for octal rings and strain is designated by the superscript "o".

$$\varepsilon_t^{c\ \max} = \varepsilon_c^{c\ \max} = \pm\frac{1.09F_zD}{2EWT^2} \tag{3}$$

$$\varepsilon_t^{o\ \max} = \varepsilon_c^{o\ \max} = \pm\frac{0.7F_zD}{2EWT^2} \tag{4}$$

where E is modulus of elastically [N/mm^2].

Fig. 5 compares the average values of the theoretical strains, $\varepsilon_{t,c}^{c\ \max}$ and $\varepsilon_{t,c}^{o\ \max}$, for each level of each design parameter as described earlier for Fig. 4. Fig. 5 also shows the values of $\varepsilon_t^{\max}$ and $\varepsilon_t^{\max}$ for the sake of comparison between simulated and theoretical strains. It is clear from the figure that the effects of the different levels of the different design parameters on $\varepsilon_t^{c\ \max}$ and $\varepsilon_t^{o\ \max}$ are the same as their effects on $\varepsilon_t^{\max}$ in terms of trends. However, simulated $\varepsilon_t^{\max}$ values are slightly lower than theoretical $\varepsilon_t^{o\ \max}$ values and considerably lower than $\varepsilon_t^{c\ \max}$ values. Fig. 5, also, shows that the averaged values of $\varepsilon_c^{\max}$ are located between the averaged values of $\varepsilon_c^{c\ \max}$ and those of $\varepsilon_c^{o\ \max}$ values.

Fig. 6 shows how the different levels of the design parameters affect sensitivity. From the figure, it is possible to notice that increasing H increases S_z while increasing T and W decreases it. In addition, R does not have a direct effect on S_z.

Fig. 7 shows the effects of the different levels of the design parameters on simulated and theoretically calculated ring stiffness. Theoretical ring stiffness is given for circular and octal rings using Eqs. (5) and (6) respectively [8].

$$k^c = \frac{1.78EWT^3}{D^3} \quad [\text{N/mm}^2] \tag{5}$$

$$k^o = \frac{EWT^3}{D^3} \quad [\text{N/mm}^2] \tag{6}$$

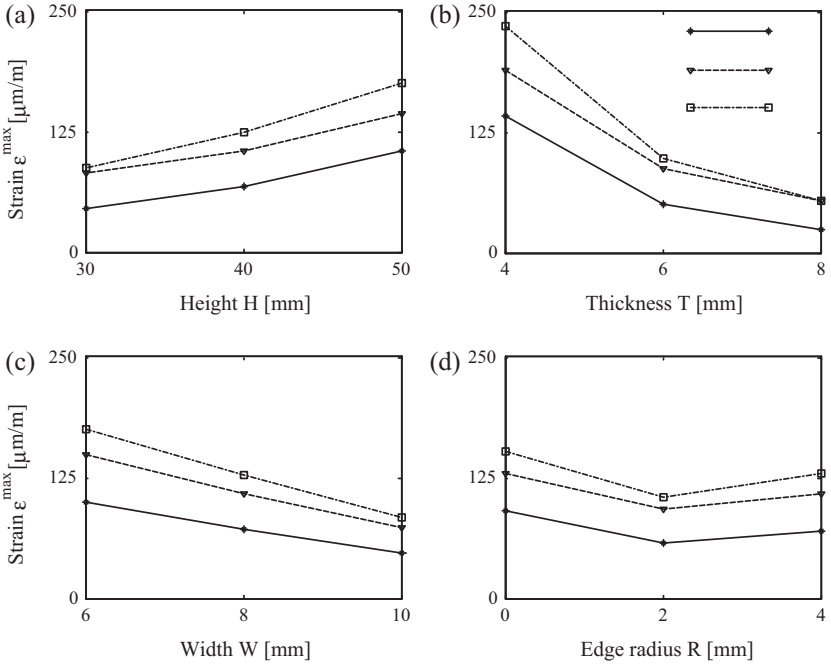

Figure 4 Effect of different levels of design parameters on maximum strains.

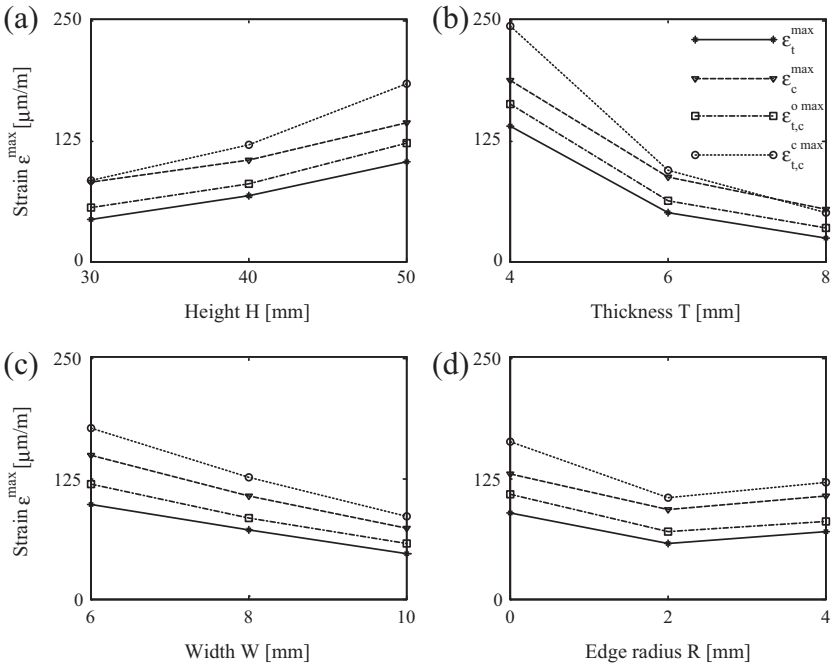

Figure 5 Simulated and theoretical effects of design parameters on maximum strains at Tm_{out}.

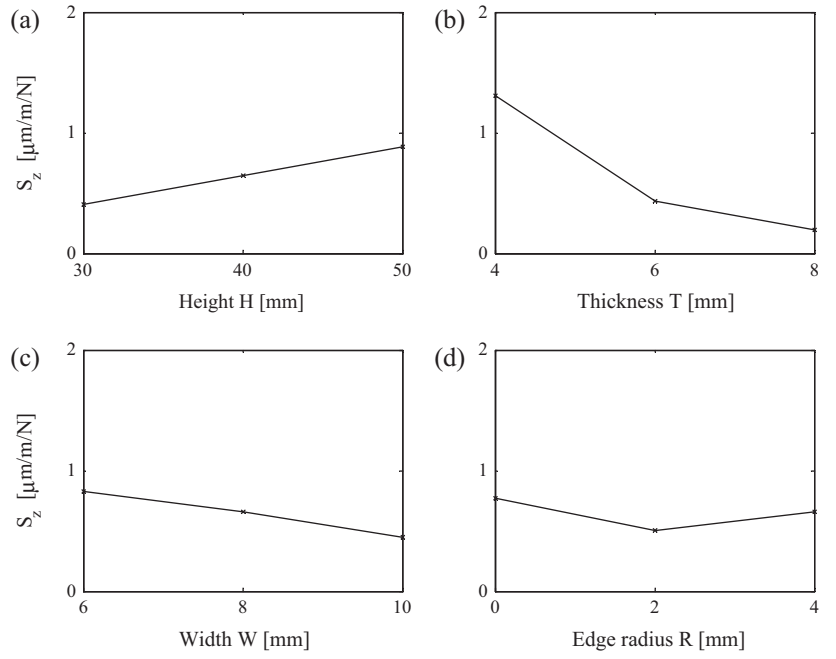

Figure 6 Effect of design parameters on strain sensitivity S_z.

From the figure, it can be seen that increasing height, H, reduces stiffness while increasing ring thickness, T, increases stiffness considerably. The width of the ring, W, does not have a direct effect of stiffness. These results are the same for simulated and theoretical results. Fig. 4d shows that increasing the edge radius reduces stiffness. Stiffness value is the highest for sharp edges, $R = 0$ [mm]. This is because edges work as obstacles to surface strain propagation from one ring face to the other. As a result, the total deflection at surface Cu_{out} is reduced.

From Figs. 2 and 3, it is clear that $\varepsilon_t^{\max}$, $\varepsilon_c^{\max}$ and $\varepsilon_u^{\max}$ take place at unique finite elements. As a result, they are practically difficult to measure using strain gauges. This is because a strain gauge has a finite length and therefore it measures the average strain within the region it adheres to. The average strain on Tm_{out}, $\varepsilon_t^{\text{avg}}$, is calculated from the equation:

$$\varepsilon_t^{\text{avg}} = \frac{1}{\text{L}_\text{g}} \int_0^{\text{L}_\text{g}} \varepsilon_t(\text{z})\text{dz} = \frac{1}{N_s} \sum_{\text{j}=1}^{N_s} \varepsilon_t(\text{j}) E_s \tag{7}$$

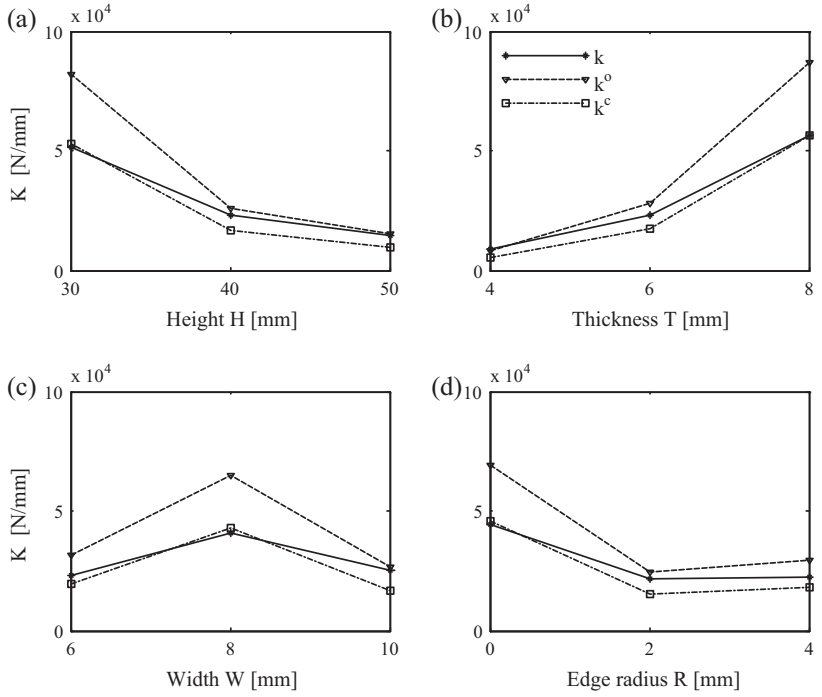

Figure 7 Simulated and theoretical effects of design parameters on maximum strains at Cm_{in}.

where L_g is the length of strain gauge and z represents the z-position of the finite element within the gauge length at which strain values are $\varepsilon_t(j)$. The average strains $\varepsilon_t^{\text{avg}}$ and $\varepsilon_t^{\text{avg}}$ are determined using similar equations, however, while the z-position is used for strain gauges at Tm_{out} and Cu_{in} the x-position is used for strain gauge at Tu_{in}. The number of finite elements on Tm_{out} and within the length of the strain gauge, L_g, is N_s. Eq. (8) gives N_s as:

$$N_s = \frac{L_g}{E_s} \tag{8}$$

The strain gauge adheres to the strain ring so that the middle of the strain gauge is at the zero z-position for Tm_{out} and Cu_{in} and at zero x-position for Tu_{in}. It is evident from Eq. (7) that the length of strain gauge affects the determination of $\varepsilon_t^{\text{avg}}$ and consequently affects $\varepsilon_c^{\text{avg}}$ and $\varepsilon_u^{\text{avg}}$.

Fig. 8 shows the effect of L_g on $\varepsilon_{t,c,u}^{\text{avg}}$ for simulations 1, 2, 4 and 7. From figure, it is clear that increasing L_g decreases $\varepsilon_{t,c,u}^{\text{avg}}$. This is because there is a variation in the strain along the length of the gauge and the consequently the gauge gives an indication of the average strain value. It is also clear from

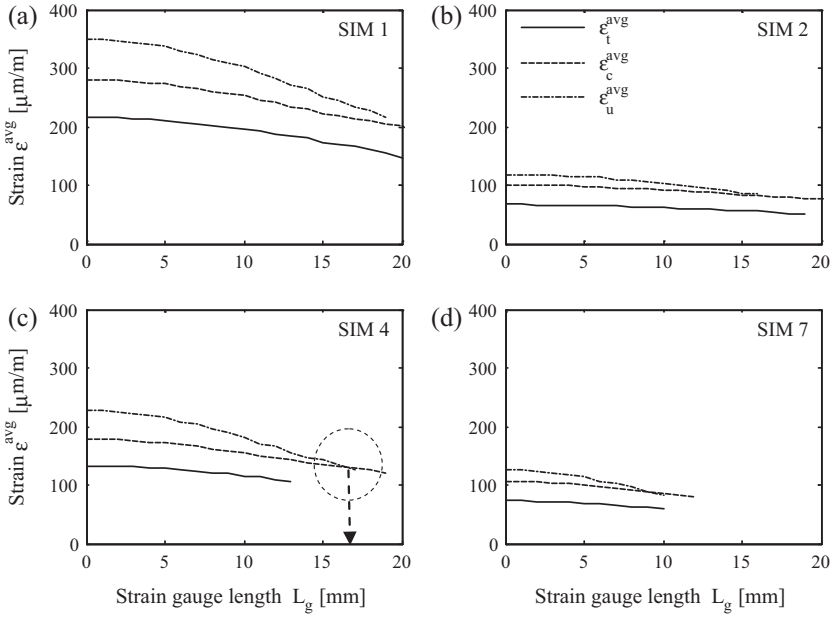

Figure 8 Effect of gauge length on average strain.

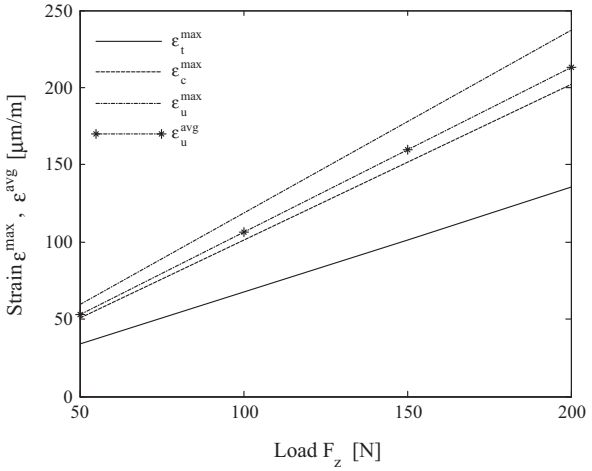

Figure 9 Effect of load F_z on maximum strain.

the figure that there is a length of strain gauge at which ε_c^{avg} and ε_u^{avg} are equal, 17 mm for simulation 4 as an example. Such length is the optimum design length of the strain gauge for the octal ring of simulation 4. This is because such length will result in equal tensile and compressive strains in the arms of the bridge connected to the ring. As a result, the nonlinearity of the force sensor is reduced.

Fig. 9 shows the effects of F_z on $\varepsilon_{t,c,u}^{max}$ and ε_u^{avg} for SIM 2. From the figure, it is evident that $\varepsilon_{t,c,u}^{max}$ and ε^{avg} are linearly proportional to load. The average strain ε^{avg} is given for a strain gauge length $L_g = 9$ [mm]. It is lower than ε_u^{max} for all load values. The figure also shows that increasing the load increases the difference between ε_u^{max} and ε_u^{avg}. This implies that the load affects strain distribution as well as the maximum strain value.

6. Conclusions

In the present work, an L_9 orthogonal array of finite element simulations was used to explore unique characteristics of octal rings and to correlate their design parameters and performance measures. Simulation results showed a considerable variation in strain along ring faces and average strain was practical to measure rather than maximum strain. An equation was developed to correlate average and maximum strains based on length of strain gauge. The equation and model simulations provided an optimum gauge length at which the tensile and compressive strains are equal, thus reducing nonlinearity of force sensors using octal rings. The optimum length depends on the design parameters of the ring. In addition, simulation results revealed a region of large tensile strain within the ring that was not exploited in the literature. Applying variation of means method to simulation results showed that increasing ring height and decreasing its thickness increase ring sensitivity and decrease ring stiffness. The width of the ring does not have clear effect of stiffness. However, increasing width decreases sensitivity. Increasing ring edge radius decreases ring stiffness but has no effect on sensitivity.

Acknowledgments

Financial support of this work through the Deanship of scientific research, Salman AbdulAziz University, under project 8/T/33 is gratefully acknowledged.

References

[1] M. Korencke, M.L. Hull, A method for designing multi-load component dynamometers incorporating octagonal strain rings, J. Experim. Mech. (1989) 195–204.
[2] Jeong-Du Kim, Dang-Sik Kim, Development of a combined-type tool dynamometer with a piezo-film accelerometer for an ultra-precision lathe, J. Mater. Process. Technol. 71 (1997) 360–366.
[3] Ulvi Seker, Abdullah Kurt, Ibrahim Ciftci, Design and construction of a dynamometer for measurement of cutting forces during machining with linear motion, J. Mater. Des. 23 (2002) 355–360.
[4] Ihsan. Korkot, A dynamometer design and its construction for milling operation, J. Mater. Des. 24 (2003) 631–637.
[5] Sedat. Karabay, Analysis of drill dynamometer with octagonal ring type transducers for monitoring of cutting forces in drilling and allied process, J. Mater. Des. 28 (2007) 673–685.
[6] Suleyman Yaldiz, Faruk Unsacar, Design, development and testing of a turning dynamometer for cutting force measurement, J. Mater. Des. 27 (2006) 839–846.
[7] Suleyman Yaldiz, Faruk Unsacar, A dynamometer design for measurement the cutting forces on turning, J. Measur. 39 (2006) 80–89.
[8] Y. Chen, N.B. McLaughlin, S. Tessier, Double extended octagonal ring (DEOR) drawbar dynamometer, J. Soil Tillage Res. 93 (2007) 462–471.
[9] Sadat Karabay, Analysis of drill dynamometer with octagonal ring type transducers for monitoring of cutting forces in drilling and allied process, J. Mater. Des. 28 (2007) 673–685.
[10] Sadat Karabay, Design criteria for electro-mechanical transducers and arrangement for measurement of strains due to metal cutting forces acting on dynamometers, J. Mater. Des. 28 (2007) 496–506.
[11] Sadat Karabay, Performance testing of a constructed drilling dynamometer by deriving empirical equations for drill torque and thrust on SAE 1020 steel, J. Mater. Des. 28 (2007) 1780–1793.
[12] Suleyman Yaldiz, Faruk Unsacar, Haci Saglam, Hakan Isik, Design development and testing of a four-component milling dynamometer for the measurement of cutting force and torque, J. Mech. Syst. Signal Process. 21 (2007) 1499–1511.